On the role of topological complexity in spontaneous development of current sheets

Sanjay Kumar[1], R. Bhattacharyya[1], and P. K. Smolarkiewicz[2]

[1] *Udaipur Solar Observatory, Physical Research Laboratory, Dewali, Bari Road, Udaipur-313001, India and*

[2] *European Centre for Medium-Range Weather Forecasts, Reading RG2 9AX, UK.*

(Dated: July 16, 2015)

Abstract

The computations presented in this work aim to asses the importance of field line interlacing on spontaneous development of current sheets. From Parker's magnetostatic theorem such development of current sheets is inevitable in a topologically complex magnetofluid, with infinite electrical conductivity, at equilibrium. Relevant initial value problems are constructed by superposition of two untwisted component fields, each component field being represented by a pair of global magnetic flux surface. The intensity of field line interlacing is then specified by the relative amplitude of the two superposed fields. The computations are performed by varying this relative amplitude. Also to have a direct visualization of current sheet formation, we follow the evolution of flux surfaces instead of the vector magnetic field. An important finding of this paper is in the demonstration that initial field lines having intense interlacing tend to develop current sheets which are distributed throughout the computational domain with no preference for topologically favorable sites like magnetic nulls or field reversal layers. The onsets of these current sheets are attributed to favorable contortions of magnetic flux surfaces where two oppositely directed parts of the same field line or different field lines come to close proximity. However, for less intensely interlaced field lines, the simulations indicate development of current sheets at sites only where the magnetic topology is favorable. These current sheets originate as two sets of anti-parallel complimentary field lines press onto each other.

PACS numbers: 52.25.Xz, 52.30.Cv, 52.35.Vd, 95.30.Qd

Keywords: MHD, Current Sheet, Magnetic flux surface, EULAG

I. INTRODUCTION

According to Parker's magnetostatic theorem [1–4], formation of tangential discontinuities, or current sheets (CSs), is inevitable in an equilibrium magnetofluid with infinite electrical conductivity and complex magnetic topology. This development of CSs is attributed to a general failure of magnetic field in achieving force balance everywhere and simultaneously preserving its topology, while remaining spatially continuous. Such CSs also develop in a magnetofluid undergoing topology preserving evolution toward an equilibrium, if the topology is complex. This requirement of topological complexity in onset of CSs is inherent to the magnetostatic theorem. In its skeletal form, the theorem utilizes relaxation of a magnetofluid with infinite electrical conductivity and low plasma β to obtain a terminal magnetic field $\mathbf{B}$ satisfying

$$\nabla \times \mathbf{B} = \alpha(\mathbf{r})\mathbf{B}, \tag{1}$$

where $\alpha(\mathbf{r})$ is a scalar function of position and represents magnetic circulation per unit flux [3]. The solenoidality of $\mathbf{B}$ further restricts $\alpha(\mathbf{r})$ to obey

$$\mathbf{B} \cdot \nabla\alpha(\mathbf{r}) = 0, \tag{2}$$

resulting in the stringent condition that the magnetic circulation per unit flux for each magnetic field line (MFL) is constant along that MFL. It is then expected that different MFLs located at the neighborhood of a given field line will be wrapped around it. An extension of this wrapping to every MFL leads to interlaced field lines, which we identify as a measure of topological complexity. From (1) it is straightforward to identify this interlacing with a non-zero field-aligned current quantified by $\mathbf{J}\cdot\mathbf{B}$, where $\mathbf{J} = \nabla\times\mathbf{B}$ is the total volume current density. Further arguments establish these MFLs satisfying (1) to have opposite chiralities at different locations and thereby violate the constancy of $\alpha(\mathbf{r})$ along a field line. The magnetostatic theorem provides a circumvention of this violation by generating CSs across which the magnetic field is discontinuous. Notably, the ubiquity of (2) associates a connotation of spontaneity to the development of these CSs.

Such spontaneous development of CSs is also intuitive in an evolving magnetofluid with infinite electrical conductivity where the Alfvèn 's flux-freezing theorem [5] is satisfied and MFLs at every instant are tied to fluid parcels. The evolution of a surface generated by the

loci of these field lines, a magnetic flux surface (MFS), is then identical in motion to a fluid surface identified by the fluid parcels to which these MFLs are tied. Under forcing, this fluid surface along with the corresponding MFS contorts, and develops CSs if the contortion is favorable [9]. In high Reynolds number ($R_M = vL/\eta$, in usual notations) magnetofluids like astrophysical plasmas, the CSs are natural sites where the magnetofluid gets locally diffusive because of a reduction in characteristic length L. The MFLs across a CS then undergo magnetic reconnection (MR), generating mass outflow and heat [4]. After reconnection, the condition of flux-freezing is restored, resulting in an expunge of reconnected MFLs frozen to the mass outflow. These reconnected field lines push onto other MFLs and may create secondary CSs which lead to further reconnections. In a recent numerical demonstration [6], this formation of secondary CSs and subsequent reconnections were identified as a possible cause for generating various magnetic structures, some duplicating magnetic antics of the Sun. The process of secondary CS development and their decay through MRs, is then expected to be continued — intermittent in space and time — until the magnetic energy achieves an allowable lower bound. In Taylor's theory of single-fluid relaxation this lower bound of the magnetic energy is determined by an approximate preservation of magnetic helicity [7], leading to a terminal state characterized by (1) but with a constant α. More general magnetohydrodynamic relaxation theories, of which the Taylor relaxation is a special case; can be formulated by using two-fluid MHD equations. The details can be found in [8] and references therein. These two complementary processes, the development of CSs and the following relaxation through MRs, may account for dynamically shaping up the magnetic topology of high R_M magnetofluids.

With the above scenario in mind, it is important to assess the role of magnetic topology, quantified by the intensity of filed line interlacing, in determining potential sites for MRs through formation of CSs. In a recent numerical work [9] these sites of CSs are found to be away from any two or three dimensional magnetic nulls with contortions of MFSs being responsible for their development. While in another set of numerical experiments [10, 11], the locations of CS formation are identified to be either at the immediate neighborhood of magnetic nulls or across magnetic field reversal layers. Since development of CSs at favorable locations lacks the notion of spontaneity, it is then indicative that formation of CSs away from either the nulls or field-reversal layers are in better agreement with the magnetostatic theorem. Thus, a plausibility is to divide numerical demonstrations of CS formation into

two broad categories. The one consists of the CSs developing at the favorable locations, and the other of CSs distributed throughout the computational domain with no apparent preference for location. Against the above backdrop, the objective is to relate intensity of interlacing with properties of developing CSs within the scope of the above two categories.

To achieve this objective, we track viscous relaxation of an incompressible, thermally homogeneous magnetofluid with infinite electrical conductivity; as it successfully demonstrates CS formation in diverse magnetic topologies with different boundary conditions. The dynamics is determined by the MHD Naviar-Stokes equations

$$\rho_0 \left(\frac{\partial \mathbf{v}}{\partial t} + (\mathbf{v} \cdot \nabla)\, \mathbf{v} \right) = \mu_0 \nabla^2 \mathbf{v} + \frac{1}{4\pi} (\nabla \times \mathbf{B}) \times \mathbf{B} - \nabla p, \tag{3}$$

$$\nabla \cdot \mathbf{v} = 0, \tag{4}$$

$$\frac{\partial \mathbf{B}}{\partial t} = \nabla \times (\mathbf{v} \times \mathbf{B}), \tag{5}$$

$$\nabla \cdot \mathbf{B} = 0, \tag{6}$$

in standard notations, where ρ_0 and μ_0 are uniform density and coefficient of viscosity respectively. For simplification, we consider only the systems periodic in all three Cartesian co-ordinates. From an initial nonequilibrium, this magnetofluid is allowed to relax toward a terminal state by converting magnetic energy W_M to kinetic energy W_K via

$$\frac{dW_K}{dt} = \int \frac{1}{4\pi} [(\nabla \times \mathbf{B}) \times \mathbf{B}] \cdot \mathbf{v}\ d^3x - \int \mu_0 \left| \nabla \times \mathbf{v} \right|^2\ d^3x, \tag{7}$$

$$\frac{dW_M}{dt} = - \int \frac{1}{4\pi} [(\nabla \times \mathbf{B}) \times \mathbf{B}] \cdot \mathbf{v}\ d^3x, \tag{8}$$

$$\frac{dW_T}{dt} = - \int \mu_0 \left| \nabla \times \mathbf{v} \right|^2\ d^3x, \tag{9}$$

the integrals being over a full period. Since the Lorentz force is conservative, the kinetic energy is dissipated via viscous drag. In absence of magnetic diffusivity, the condition of flux-freezing holds and the end state is expected to be in magnetostatic equilibrium, identical in magnetic topology to the initial state. The magnetostatic theorem then demands spontaneous development of CSs in the terminal state if the initial magnetic field is topologically complex, which we ensure by constructing relevant initial value problems (IVPs).

We organize the paper in the following order. In section II we introduce the relevant IVPs, while numerical model is discussed in section III. The section IV is dedicated to results and

discussions. In section V we summarize these results and highlights the important findings.

II. INITIAL VALUE PROBLEM

The initial value problem is constructed by realizing that a magnetic field with non-interlaced field lines can be written as [10, 14]

$$\mathbf{B}_1 = W(\psi_1, \phi_1)\nabla\psi_1 \times \nabla\phi_1, \tag{10}$$

where ψ_1 and ϕ_1 are two scalar functions of position, known as Euler Potentials (EP) [12, 13] and the amplitude W is an explicit function of ψ_1 and ϕ_1. The solenoidality of $\mathbf{B}_1$ is evident from the above expression. Because the field aligned current $\mathbf{J}_1 \cdot \mathbf{B}_1 = 0$, the field lines of $\mathbf{B}_1$ are closed curves. In addition, with conditions $\mathbf{B}_1 \cdot \nabla\psi_1 = \mathbf{B}_1 \cdot \nabla\phi_1 = 0$ being satisfied, level sets of ψ_1 and ϕ_1 are global MFSs, the intersections of which generate magnetic field lines. It is noteworthy that $\mathbf{B}_1$, in general, has a nonzero $\mathbf{J}_1$ and hence although untwisted, is not a potential field. Interlaced field lines are generated by superposing $\mathbf{B}_1$ with another $\mathbf{B}_2$, represented by a separate pair of EPs $\{\psi_2, \phi_2\}$ and having an amplitude W_2. The superposed field $\mathbf{B}$ is given by

$$\mathbf{B} = \mathbf{B}_1 + \epsilon_0 \mathbf{B}_2, \tag{11}$$

$$= (\nabla\psi_1 \times \nabla\phi_1) + \epsilon_0 (\nabla\psi_2 \times \nabla\phi_2), \tag{12}$$

where the amplitudes $W_1 = W_2 = 1$ and the constant ϵ_0 is related to the intensity of interlacing. Notably, a representation of any magnetic field by superposition of two untwisted or non-interlaced component fields is not general enough, and at least three such component fields are required to represent an arbitrary magnetic field; cf. recent review [14]. Our specific choice (11) of two component fields for the purpose of superposition is based only on having a single parameter ϵ_0 to alter the intensity of interlacing. Based on our previous work [9], we select the following EPs

$$\psi_1(x, y, z) = a_0 \cos x \sin z, \tag{13}$$

$$\phi_1(x, y, z) = a_0 \cos y, \tag{14}$$

and

$$\psi_2(x, y, z) = a_0 \sin x \sin y, \tag{15}$$

$$\phi_2(x, y, z) = -a_0 \cos z, \tag{16}$$

with an amplitude a_0 and defined in an uniform triply periodic Cartesian domain of period 2π. Figures 1(a) and 1(b) illustrate the level sets of the above EPs in pairs, (ψ_1, ϕ_1) and (ψ_2, ϕ_2) respectively for $a_0 = 1$, with ψ-constant surfaces in color grey and ϕ-constant surfaces in color red. The closed lines generated by intersection of the two surfaces are MFLs which are untwisted, as can easily be verified from their appearances. To further facilitate visualization, we overlay Figure 1 with $y = \pi$ plane depicted in color green. Also, in this and subsequent figures, the arrows in colors red, green, and blue depict the directions x, y, and z respectively.

From (12), the initial component fields $\mathbf{H}_1 = \{H_{1x}, H_{1y}, H_{1z}\}$ and $\mathbf{H}_2 = \{H_{2x}, H_{2y}, H_{2z}\}$ are

$$H_{1x} = {a_0}^2 \cos x \sin y \cos z, \tag{17}$$

$$H_{1y} = 0, \tag{18}$$

$$H_{1z} = {a_0}^2 \sin x \sin y \sin z, \tag{19}$$

and

$$H_{2x} = {a_0}^2 \sin x \cos y \sin z, \tag{20}$$

$$H_{2y} = -{a_0}^2 \cos x \sin y \sin z, \tag{21}$$

$$H_{2z} = 0. \tag{22}$$

The superposed field $\mathbf{H} = \{H_x, H_y, H_z\}$ is

$$H_x = {a_0}^2 \left(\cos x \sin y \cos z + \epsilon_0 \sin x \cos y \sin z\right), \tag{23}$$

$$H_y = -{a_0}^2 \left(\epsilon_0 \cos x \sin y \sin z\right), \tag{24}$$

$$H_z = {a_0}^2 \left(\sin x \sin y \sin z\right). \tag{25}$$

The Lorentz force exerted by $\mathbf{H}$ is

$$L_x = {a_0}^4\left[\left(\epsilon_0^2 - 1\right)\sin 2x \sin^2 y \sin^2 z - \left(\frac{\epsilon_0}{4}\right)\cos 2x \sin 2y \sin 2z\right], \tag{26}$$

$$L_y = {a_0}^4\left[\left(\epsilon_0^2 - \frac{1}{2}\right)\sin^2 x \sin 2y \sin^2 z - \left(\frac{\epsilon_0}{4}\right)\sin 2x \cos 2y \sin 2z - \left(\frac{1}{2}\right)\cos^2 x \sin 2y \cos^2 z\right], \tag{27}$$

$$L_z = -{a_0}^4\left[\left(\frac{\epsilon_0^2}{2} - 1\right)\cos^2 x \sin^2 y \sin 2z + \left(\frac{\epsilon_0}{4}\right)\sin 2x \sin 2y \cos 2z + \left(\frac{\epsilon_0^2}{2}\right)\sin^2 x \cos^2 y \sin 2z\right]. \tag{28}$$

Noting the initial Lorentz force to be a function of ϵ_0, the amplitude a_0 is adjusted to perform computations with initial fields having different ϵ_0 but identical magnitude of average Lorentz force.

The field-aligned current density and the global magnetic helicity for $\mathbf{H}$ are

$$(\nabla \times \mathbf{H}) \cdot \mathbf{H} = {a_0}^4 \epsilon_0 (\sin^2 x \cos^2 y \sin^2 z + \cos^2 x \sin^2 y \cos^2 z + 2\sin^2 y \sin^2 z), \tag{29}$$

$$K_M = 2{a_0}^4 \epsilon_0 \pi^3, \tag{30}$$

which reveal that they are directly proportional to ϵ_0. The global magnetic helicity is calculated here using the classical expression

$$K_M = \int \mathbf{A} \cdot \mathbf{H} dV, \tag{31}$$

with $\mathbf{A}$ as vector potential, the integral being over a full period, and a constant gauge. Discussions on K_M for more general cases can be found in [15] and [16]. The global magnetic helicity is a measure of interlinkages between MFLs and hence, is explicitly related to interlacing of field lines. The direct proportionality to ϵ_0 in (29) and (30) is affirmative of an increase in interlacing, and hence making MFLs of $\mathbf{H}$ more topologically complex. The above inference can further be validated from Figure 2 which visually clarifies an increase of interlacing in MFLs with ascending values of ϵ_0.

To facilitate presentation, in the following we discuss the topology of $\mathbf{H}$ in relation to ϵ_0. In Figure 3, we plot MFLs of $\mathbf{H}$ for four separate values: $\epsilon_0 = \{0.1, 0.3, 0.5, 0.7\}$ in the vicinity of $y = \pi$ plane. Features evident in this figure are helical MFLs for $\epsilon_0 = 0.1$, and the

deviation of MFLs from this helical structure with an increase of ϵ_0 culminating into MFLs depicted in panels b, c and d. To explain these features we revert to equations (23)-(25) and note that for $\epsilon_0 = 0$, the field lines of $\mathbf{H}$ are closed disjoint curves tangential to y-constant planes (since the component H_y is zero). For any other ϵ_0, the component field $\mathbf{H}_2$ provides a nonzero H_y resulting in lifting up MFLs of $\mathbf{H}$ out of the y constant planes. In addition, a nonzero ϵ_0 contributes to the component H_x. The net result is then a deformation of MFLs in directions both perpendicular and parallel to y-constant planes. For a small value of ϵ_0 this deformation is also small, resulting in helical field lines with projections on y-constant planes similar in geometry to the closed curves of $\epsilon_0 = 0$. Larger values of ϵ_0 deform field lines more, leading to MFLs depicted in panels b, c and d. A first order Taylor expansion of equations (23)-(25) near the $y = \pi$ plane for constant x and z yields

$$H_x = -{a_0}^2 \epsilon_0 \sin x_0 \sin z_0 - {a_0}^2 (y - \pi) \cos x_0 \cos z_0, \tag{32}$$

$$H_y = {a_0}^2 \epsilon_0 (y - \pi) \cos x_0 \sin z_0, \tag{33}$$

$$H_z = -{a_0}^2 (y - \pi) \sin x_0 \sin z_0, \tag{34}$$

evincing H_y and H_z to flip sign across the $y = \pi$ plane. However for $\epsilon_0 \neq 0$, H_x flips sign at $y = \pi - y_1$ where y_1 satisfies the condition

$$y_1 > \frac{\epsilon_0 \sin x_0 \sin z_0}{\cos x_0 \cos z_0}. \tag{35}$$

A pair of oppositely directed MFLs across $y = \pi$ plane are shifted by y_1, which in turn increases with ϵ_0 (Fig. 3), rendering an initial $\mathbf{H}$ with larger ϵ_0 less favorable to develop CSs.

Further insight into topology of the initial field is gained by constructing its skeleton in terms of magnetic nulls, since these are the sites where development of CSs are expected. To illustrate the nulls, following [11] we employ the condition $\mathbf{H} \equiv \{H_x,\ H_y,\ H_z\} = 0$ in a Gaussian construct

$$\chi(x, y, z) = exp\left[- \sum_{i=x,y,z} \frac{(H_i(x, y, z) - H_0)^2}{d_0} \right]. \tag{36}$$

where $\sqrt{d_0}$ determines width of the Gaussian and H_0 represents a particular isovalue of $H_x, H_y,$ and H_z. By choosing $H_0 \approx 0$ and a small d_0, the function $\chi(x, y, z) \neq 0$ only

if $H_i \approx H_0$ for each i. The three dimensional (3D) nulls are the points where the three isosurfaces $H_x = H_0, H_y = H_0, H_z = H_0$ intersect. It should be noted that at the immediate vicinity of a 3D null all the three components of magnetic field is nonzero. Similarly, a two dimensional (2D) null in a 3D coordinate space can be described as a line of intersection between H_0 isosurfaces of two nonzero magnetic field components while the third component is trivially zero at this line. Using the above technique, in Figure 4 we have depicted nulls of $\mathbf{H}$ for $\epsilon_0 = 0.5$ by selecting parameters $H_0 = 0.01$ and $d_0 = 0.05$. The accuracy of the depiction can easily be verified from the analytical expression of $\mathbf{H}$ in equations (23)-(25). The Figure 4 straightaway confirms only the presence of 2D nulls in the form of lines and a complete absence of 3D nulls. Similar results (not shown) are obtained for the other ϵ_0 values.

To further identify the 2D nulls, we expand components of $\mathbf{H}$ in a Taylor series in the immediate vicinity of $x = \pi/2, z = \pi$ for a constant y to get

$$H_x = {a_0}^2 \left(x - \frac{\pi}{2}\right) \sin y_0 - {a_0}^2 (z - \pi)\, \epsilon_0 \cos y_0, \tag{37}$$

$$H_y = 0, \tag{38}$$

$$H_z = -{a_0}^2 (z - \pi) \sin y_0. \tag{39}$$

Notably, the non-zero components H_x and H_z have point antisymmetry about co-ordinates $x = \pi/2, z = \pi$ along the y-line rendering every point on it to be a X-type neutral point. The MFLs near two such neutral points are shown in the inset (Fig. 4). Similarly the z-line (extending in z-direction) is also X-type neutral line. Moreover, the Taylor series expansion of components field in the immediate neighborhood of $y = \pi, z = \pi$ for a constant x yields,

$$H_x = {a_0}^2 (y - \pi) \cos x_0 - {a_0}^2 (z - \pi)\, \epsilon_0 \sin x_0, \tag{40}$$

$$H_y = 0, \tag{41}$$

$$H_z = 0, \tag{42}$$

thus confirming the line along the x-axis with co-ordinates $y = z = \pi$ to be a neutral line.

III. NUMERICAL MODEL

Under the condition of flux freezing, the time evolution of the EPs ψ_i, ϕ_i $(i = 1, 2)$ are governed by simple advection equations [9, 10]

$$\frac{d\psi_i}{dt} = 0, \tag{43}$$

$$\frac{d\phi_i}{dt} = 0, \tag{44}$$

implying

$$\frac{\partial\psi_i}{\partial t} + \mathbf{v} \cdot \nabla\psi_i = 0, \tag{45}$$

$$\frac{\partial\phi_i}{\partial t} + \mathbf{v} \cdot \nabla\phi_i = 0. \tag{46}$$

Any numerical calculation utilizing advection of MFSs requires satisfaction of the flux-freezing condition to a high fidelity. The computational requirement is then a minimization of numerically generated dissipation and dispersion errors. Such a minimization is a signature of a class of inherently nonlinear "high-resolution" transport methods that conserve field extrema along flow trajectories while ensuring higher order accuracy away from steep gradients in the advected fields. For our calculations we adapt the MHD version [17] of the well established general-purpose hydrodynamic model EULAG predominantly used in atmospheric and climate research [18, 19].

For completeness, here we summarize only the crucial features of the EP based MHD version of the EULAG; the details are in [10]. This model is based on the spatio-temporally second order accurate nonoscillatory forward-in-time (NFT) advection scheme MPDATA (Multidimensional Positive Definite Advection Transport Algorithm) [19]. A feature important to MPDATA and relevant to our calculations is its proven dissipative property which is intermittent and adaptive to generation of under-resolved scales in field variables for a fixed grid resolution. As the CS develops, the magnetic field gradient increases unboundedly and a fixed grid resolution becomes insufficient in presence of these high gradients. The MPDATA then removes these under-resolved scales by generating a locally-effective residual dissipation of the second order, sufficient to maintain solution monotonicity. This intermittency and adaptiveness is effective in implicit large-eddy simulation (ILES) that mimics the

action of explicit subgrid-scale turbulence models, whenever the concerned advective field is under-resolved [20]. Utilizing this ILES scheme, Ghizaru and coworkers have successfully simulated regular solar cycles [21], while rotational torsional oscillations in a global solar dynamo were characterized and analyzed [22]. The present understanding along with, open questions on modeling the solar dynamo are summarized in reference [23]. Furthermore, in the recent works [6, 11], this ILES mode was successfully used to obtain numerically induced MRs that lead to secondary CSs. In the present computations, we follow evolution of MFSs until onsets of such MRs to ensure satisfaction of the flux-freezing to a high fidelity.

IV. RESULTS AND DISCUSSIONS

The results are presented for numerical computations carried out with zero initial velocity and ϵ_0 in the range of $\{0.1, 0.7\}$, in steps of 0.1. The computational grid has uniform resolution of 128^3 and corresponds to a physical volume of $(2\pi)^3$. The coefficient of viscosity and the mass density are set to $\mu_0 = 0.008$ and $\rho_0 = 1$ respectively. When released from an initial non-equilibrium state, the dynamics develops because of an imbalance between the Lorentz force and the pressure gradient with zero initial value. The resulting increase in velocity gets arrested by viscous drag and the magnetofluid relaxes toward a quasi-steady state while preserving its magnetic topology. For a general understanding of this viscous relaxation, Figure 5 plots the histories of kinetic and magnetic energies for $\epsilon_0 = 0.1$, normalized to the initial total (magnetic +kinetic) energy. The development of the peak in kinetic energy centered at $t = 20s$ is due to the viscous arrest. The quasi-steady phase of the evolution is in the temporal range $t \in \{60s, 120s\}$ and is characterized by an almost constant kinetic energy, while the change in magnetic energy is restricted to 13% of its total variation. For other values of ϵ_0, the magnetic and kinetic energy curves show the same qualitative behavior but with different timing and amplitudes (not shown).

The accuracy of computations is assessed in Figure 6 displaying numerical deviations of normalized kinetic (dashed line) and magnetic (solid line) energy rates from their analytical values in (7) and (8). The displayed deviations are for different ϵ_0 values: $\epsilon_0 = 0.1, 0.3, 0.5,$ and 0.7, which we have selected as the representative cases. The plots confirm the numerical accuracy to be maintained with acceptable precision; the maximal deviation being 0.0002 (panel d). This accurate maintenance of energy rates denies any possibility of numerical MRs

and hence, confirms the preservation of magnetic topology throughout the computations.

The overall tendency to form CSs can be established from panels a and b of Figure 7, plotting the evolution of average total current density $<|\ \mathbf{J}\ |>$ and maximal value of $|\ \mathbf{J}\ |$ respectively. We denote the latter by $J_{\max}$ and the current densities in the plots are normalized to their initial values. Notable is their tendency to increase, albeit without monotonicity, from the respective initial values. Because for every ϵ_0 the average component current density $<|\ \mathbf{J}_2\ |>=<|\ \nabla \times \mathbf{H}_2\ |>$ shows a monotonous increase, and the scalar product $< \mathbf{J}_1 \cdot \mathbf{J}_2 >$ (where $\mathbf{J}_1 = \nabla \times \mathbf{H}_1$) remains negative (cf. panels a and b of Fig. 8) throughout evolution, this lack of monotonicity in $<|\ \mathbf{J}\ |>$ is exclusively due to contribution from the $<|\ \mathbf{J}_1\ |>$ (panel c, Fig. 8). Similar analysis (not shown) yields contributions from the corresponding maximum $|\ \mathbf{J}_1\ |$ to be responsible for the lack of monotonicity in $J_{\max}$.

Additional computations are performed for different uniform grid resolutions varying from 96^3 to 160^3 in steps of 16^3, with $\epsilon_0 = 0.1$ and $\epsilon_0 = 0.5$ as the representative cases. The resulting plots (Fig. 9) document scaling of $J_{\max}$ with resolution, which points in favor of CS formations [24]. Moreover, the scaling is stronger for $\epsilon_0 = 0.1$, where the $y = \pi$ plane is favorable for CS formation. In contrast, for $\epsilon_0 = 0.5$, with no apparent favorable location for CS formation, the scaling is weaker. Such comparative scaling is a signature of scenarios where CSs develop at three dimensional magnetic nulls against CSs developing away from the nulls [25–27].

To identify and locate onset of CSs, in the following we further analyze the four cases separately. The analyzes are for the computations with 128^3 grid resolution where we follow appearances and geometries of the isosurface of $|\ \mathbf{J}\ |$, referred hereafter as $J - 50$, with an isovalue which is 50% of maximum $|\ \mathbf{J}\ |$ for each ϵ_0. Also to facilitate the general understanding, we overlay these isosurfaces with magnetic nulls.

A. Case (I) $\epsilon_0 = 0.1$

The evolution of the corresponding $J - 50$ surfaces overlaid with magnetic nulls is illustrated in Figure 10. Based on their shape, these surfaces can be classified into two geometrically distinct categories: the open surfaces appearing at the $y = \pi$ plane and the elongated closed surfaces distributed sparsely in the volume. Evident from the MFL evolution depicted in Figure 11, the open surfaces are the CSs developed by two antiparallel

complimentary field lines approaching toward the $y = \pi$ plane. Additionally, the figure identifies generation of the closed $J - 50$ surfaces to an increase in the local number density of parallel field lines, resulting in an increase in $\mid \mathbf{H} \mid$ and hence $\mid \mathbf{J} \mid$. A sharpening of field gradient playing no role in the generation, the closed surfaces do not qualify as CSs.

B. Case (II) $\epsilon_0 = 0.3$

To complement results of Case I, here we analyze $J - 50$ surfaces for computation with $\epsilon_0 = 0.3$. In Figure 12, we illustrate the history of $J - 50$ surfaces overlaid with magnetic nulls. It is evident from the figure that most of the $J - 50$ surfaces are elongated closed structures similar to the case of $\epsilon_0 = 0.1$. In addition, development of localized current layers at the $y = \pi$ plane is noted. Like the previous case, here also an enhancement in density of parallel MFLs is responsible for a local increase in magnitude of $\mathbf{J}$, leading to the formation of these closed current surfaces. More importantly, Figure 12 indicates a delay in the generation of CSs in comparison to the earlier case. This is expected since the initial topology of field lines for larger ϵ_0 is less favorable and hence, two oppositely directed MFLs require additional push to onset the $J - 50$ surfaces. Also, the spatial extension of these CSs is lesser compared to the case I.

C. Case (III) $\epsilon_0 = 0.5$

With $\epsilon_0 = 0.5$, the initial favorable topology around $y = \pi$ plane is almost destroyed and the MFLs are interlaced everywhere (panel c, Fig. 2). The appearances of $J - 50$ surface (overlaid with magnetic nulls) is depicted in Figure 13. The $J - 50$ surfaces start to appear around $t = 32s$ and in their initial phase of evolution are closed surfaces, suggesting a localized increase in $\mid \mathbf{H} \mid$. With time, these closed surfaces become increasingly open; generating CSs in the form of helices extended along the y direction and patches located at the $y = \pi$ plane. Importantly these CSs are located away from the magnetic nulls.

To understand this development of CSs away from the magnetic nulls, the time evolution of appropriate Euler surfaces and selected isosurfaces of $\mid \mathbf{J}_1 \mid$ and $\mid \mathbf{J}_2 \mid$ is explored in the following. Considering the negative contribution from $\mathbf{J}_1 \cdot \mathbf{J}_2$, we set the optimal isovalues to 40% of the maximum of $\mid \mathbf{J}_1 \mid$ or $\mid \mathbf{J}_2 \mid$, depending on the component current density

under consideration. These isosurfaces are nomneclatured as $J_1 - 40$ and $J_2 - 40$ surfaces respectively. The Figure 14 illustrates a snapshot of $J_1 - 40$ surfaces at the instant $t = 112s$, displayed in the half computational domain $z \in \{0, \pi\}$. Notably, the $J_1 - 40$ surfaces are also in the forms of helices and patches (marked by downward arrows), structurally similar and co-located to the $J - 50$ surfaces. This structural similarity and co-located appearance ascertains the $J_1 - 40$ surfaces to be major contributors toward the development of $J - 50$ surfaces. The helical $J_1 - 40$ surfaces originate from favorable contortions of $\psi_1 -$ constant Euler surfaces, evident from the Figure 15. However, the patches are due to contortions of $\phi_1 -$ constant Euler surfaces near the $y = \pi$ plane (cf. Figure 16). Identical contortions of $\psi_2 -$ constant and $\phi_2 -$ constant Euler surfaces generate the corresponding $J_2 - 40$ surfaces (not shown).

D. Case (IV) $\epsilon_0 = 0.7$

In this case, the initial MFLs are interlaced more strongly (panel d, Fig. 2). To complement the findings in Case (III), in Figure 17 we depict appearances of $J - 50$ surface. Evidently, these surfaces are initially closed and hence are due to local enhancements in $|\ \mathbf{H}\ |$. Later in their evolution, these surfaces become open and morphed into CSs. In comparison to the previous case, these CSs are distributed more extensively in the computational domain and hence, signify that more intensely interlaced field lines produce CSs with lesser preference for locations; a finding which is in conformity with the magnetostatic theorem.

Figure 18 shows the $J - 50$ surfaces at $t = 112s$, plotted in the half computational domain. Like the previous case, these $J - 50$ surfaces can also be classified into helices and patches (marked by the upward arrows). To explain their origin, in Figure 19 we illustrate the corresponding $J_1 - 40$ surface at the instant $t = 112s$. The figure confirms, the helical $J - 50$ surfaces owe their origin to a development of $J_1 - 40$ surfaces. Further, Figure 20 relates the onset of these $J_1 - 40$ surfaces to contortions of $\psi_1 -$ constant Euler surfaces. The development of the patches is attributed to $J_2 - 40$ surfaces, as suggested by Figure 21 that depicts evolution of a single $J_2 - 40$ surface located at the immediate vicinity of a patch. The figure is overlaid with evolution of $\phi_2 -$ constant Euler surfaces co-located to the $J_2 - 40$ surface. From the figure, it is clear that the onset of $J_2 - 40$ surfaces are due to

contortions of the $\phi_2 -$ constant Euler surface.

In view of the above discussion, the comparative scaling documented in Figure 9, can now be put into its proper perspective. The intensity of CSs developing at favorable locations (cases I and II) have stronger scaling with resolution than the intensity of CSs that develop in absence of favorable locations (cases III and IV). In a recent work, Craig and Effenberger [25] found similar comparative scaling in the scenario of CS formation at 3D nulls against CS formation at quasi-separatrix layers (QSLs). The QSLs are regions where the magnetic connectivity between a pair of boundaries changes drastically [28]. Along with separators [29, 30], QSLs are known to be the sites, away from nulls, where CSs can develop [25, 31]. It is then imperative to seek QSLs in $\mathbf{H}$ and their relation to CS formation.

In Figure 22, we plot MFLs at the immediate vicinity of a helical CS for $\epsilon_0 = 0.5$. The plots are for instants $t = 0s$ and $t = 112s$. The figure documents the connectivity of two sets of MFLs (in colors red and cyan) connecting plane C with planes D and E. The different connectivities of the two sets are evident from the figure. With CS (marked in color blue) being co-located with the layer where the connectivity changes, existence of QSL structures containing the CS is suggested. A comparison between the two instants further reports MFLs to get more helical with development of the CS, indicating causality between the favorable contortions and the dynamics of QSLs — an important problem that demands separate work.

V. SUMMARY

In this work, we asses the importance of complexity in magnetic topology on development of CSs. The initial magnetic field is constructed by superposing two untwisted fields, where each field is represented by a pair of global magnetic flux surfaces. The magnetic field lines of the superposed field are interlaced and the intensity of interlacing increases with the relative amplitude ϵ_0 of the component fields. The particular initial field used here, enables us to divide the magnetic topology into two broad categories: one with favorable MFL geometry having complementary field lines directed anti-parallel to each other across the $y = \pi$ plane; and the other with interlaced field lines without any such favorable geometry. The numerical computations are performed in a triply periodic uniform Cartesian grid and simulate the viscous relaxation of an incompressible, thermally homogeneous magnetofluid with infinite

electrical conductivity. Moreover, to get a direct visualization of CS formation we advect magnetic flux surfaces instead of the more traditional vector magnetic field.

The numerical precision in preservation of the initial magnetic topology is ensured by the second-order-accuracy of non-oscillatory advection scheme MPDATA. The overall tendency to form CSs is confirmed by the history of component average current densities for different ϵ_0. To identify the locations of CSs in the computation domain and obtain a detail understanding, we analyze the evolution of isosurfaces of total current density having sufficiently high value. For smaller ϵ_0 (i.e. for ϵ_0=0.1 and 0.3), the analyzes establish generation of CSs at the $y = \pi$ plane which is location favorable to CS development. With an increase of ϵ_0, this favorable topology of field lines gets destroyed. For larger ϵ_0 (i.e. for ϵ_0=0.5 and 0.7), additional CSs appear which are located away from the $y = \pi$ plane and the magnetic nulls. Further analysis identifies the origin of these CSs to favorable contortions of co-located magnetic flux surfaces.

Noteworthy are the insights gained on the relation between the intensity of interlacing and the onset of CSs. We have demonstrated that a magnetic field with less interlacing develop CSs at locations where such development is topologically favorable. Also these CSs are localized at the immediate neighborhood of the favorable location. In contrast, for more interlaced field lines the CSs develop away from magnetic nulls or any such topologically favorable sites. Further, the CSs being distributed throughout the volume with spatial extensions that increase with intensity of interlacing, their development supports the magnetostatic theorem to its full generality. The onset of CSs are further found to be near possible QSLs and related to their dynamics.

Altogether, the computations reported here and in [6, 9–11] substantiate and extend the magnetostatic theorem by relating the intensity of MFL interlacing to the spatial distribution of CSs and identifying MFS contortions as the rationale behind the onset of CSs away from the favorable locations. The contortions are related to possible QSL structures which, provides a basis to extend the EP based computations to the solar corona. Combined with the scenario of secondary CS development which, in general, increases the topological complexity; the findings of this paper point toward the ubiquity of CSs in a high R_M magnetofluid. To relate this ubiquity to observation, it is crucial to include field line topologies similar to the coronal loops along with physical MRs, and this warrants a separate study.

VI. ACKNOWLEDEMENTS

The simulations are performed using the High Performance Computing (HPC) cluster and the 100 TF cluster Vikram-100 at Physical Research Laboratory, India. We also wish to acknowledge the visualisation software VAPOR (www.vapor.ucar.edu), for generating relevant graphics. One of us (PKS) is supported by funding received from the European Research Council under the European Union's Seventh Framework Programme (FP7/2012/ERC Grant agreement no. 320375). The authors also sincerely thank an anonymous reviewer for providing specific suggestions to enhance the presentation as well as to raise the academic content of the paper.

---

[1] E. N. Parker, Astronphys. J. **174**, 499 (1972).

[2] E. N. Parker, Astrophys. J. **330**, 474 (1988).

[3] E. N. Parker, Plasma Phys. Control. Fusion **54**, 124028 (2012).

[4] E. N. Parker, *Spontaneous Current Sheets Formation in Magnetic Fields* (Oxford University Press, New York, 1994).

[5] E. R. Priest, *Solar Magnetohydrodynamics* (Reidel, Dordrecht, 1982).

[6] D. Kumar, R. Bhattacharyya, and P. K. Smolarkiewicz, Phys. Plasmas **22**, 012902 (2015).

[7] J. B. Taylor, Phys. Rev. Lett. **33**, 1139 (1974).

[8] D. Kumar and R. Bhattacharyya, Phys. Plasmas **18**, 084506 (2011).

[9] S. Kumar, R. Bhattacharyya, and P. K. Smolarkiewicz, Phys. Plasmas **21**, 052904 (2014).

[10] R. Bhattacharyya, B. C. Low, and P. K. Smolarkiewicz, Phys. Plasmas **17**, 112901 (2010).

[11] D. Kumar, R. Bhattacharyya, and P. K. Smolarkiewicz, Phys. Plasmas **20**, 112903 (2013).

[12] D. P. Stern, J. Geophys. Res. **72**, 3995, doi:10.1029/JZ072i015p03995 (1967).

[13] D. P. Stern, Am. J. Phys. **38**, 494 (1970).

[14] B. C. Low, Sci China-Phys Mech Astron **58**, 015201, doi:10.1007/s11433-014-5626-7 (2015).

[15] B. C. Low, Phys. Plasmas **18**, 052901 (2011).

[16] M. A. Berger, J. Geophys. Res. **102**, 2637, doi:10.1029/96JA01896 (1997).

[17] P. K. Smolarkiewicz and P. Charbonneau, J. Comput. Phys. **236**, 608 (2013).

[18] J. M. Prusa, P. K. Smolarkiewicz, and A. A. Wyszogrodzki, Comput. Fluids **37**, 1193 (2008).

[19] P. K. Smolarkiewicz, Int. J. Numer. Methods Fluids **50**, 1123 (2006).

[20] L. G. Margolin, W. J. Rider, and F. F. Grinstein, J. Turbul. **7**, N15 (2006).

[21] M. Ghizaru, P. Charbonneau, and P. K. Smolarkiewicz, Astrophys. J. Lett. **715**, L133 (2010).

[22] P. Beaudoin, P. Charbonneau, E. Racine, and P. K. Smolarkiewicz, Sol. Phys. **282**, 335 (2013).

[23] P. Charbonneau and P. K. Smolarkiewicz, Science **340**, 42 (2013).

[24] C. Mellor, C. L. Gerrard, K. Galsgaard, A. W. Hood, and E. R. Priest, Sol. Phys. **227**, 39 (2005).

[25] I. J. D. Craig and Frederic Effenberger, Astrophys. J. **795**, 129 (2014).

[26] I. J. D. Craig and D. I. Pontin, Astrophys. J. **788**, 177 (2014).

[27] A. L. Wilmot-Smith, arXiv:1411.2490v1 (2015).

[28] E. R. Priest and P. Démoulin, J. Geophys. Res. **100**, 23443 (1995).

[29] K. Galsgaard and Å. Nordlund, J. Geophys. Res. **102**, 231 (1997).

[30] J. E. H. Stevenson, C. E. Parnell, E. R. Priest, and A. L. Haynes, Astron. Astrophys. **573**, A44 (2015).

[31] G. Aulanier, E. Pariat, and P. Démoulin, Astron. Astrophys. **444**, 961 (2005).

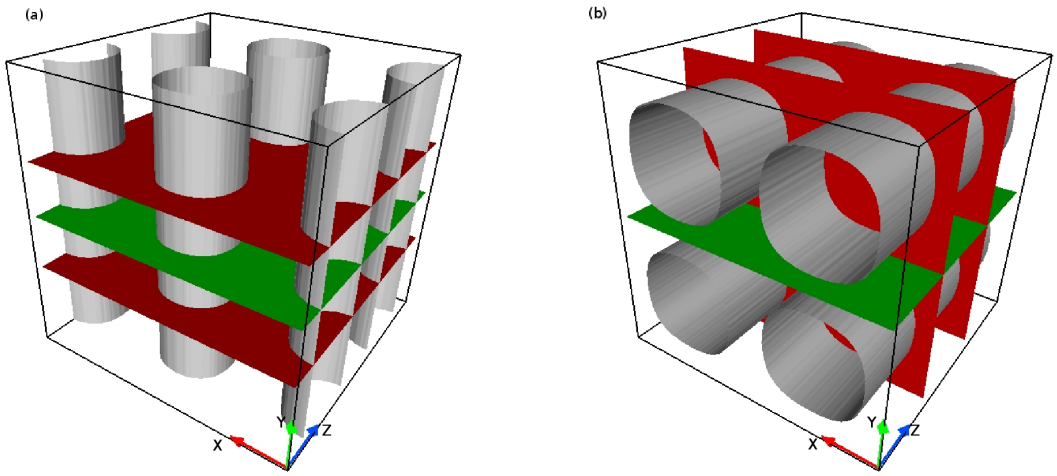

FIG. 1: Panel a depicts initial Euler surfaces $\psi_1 = \pm 0.5$ in grey and $\phi_1 = -0.35$ in red. Panel b depicts initial Euler surfaces $\psi_2 = \pm 0.1$ in grey and $\phi_2 = 0.15$ in red. The surface in green marks the $y = \pi$ plane.

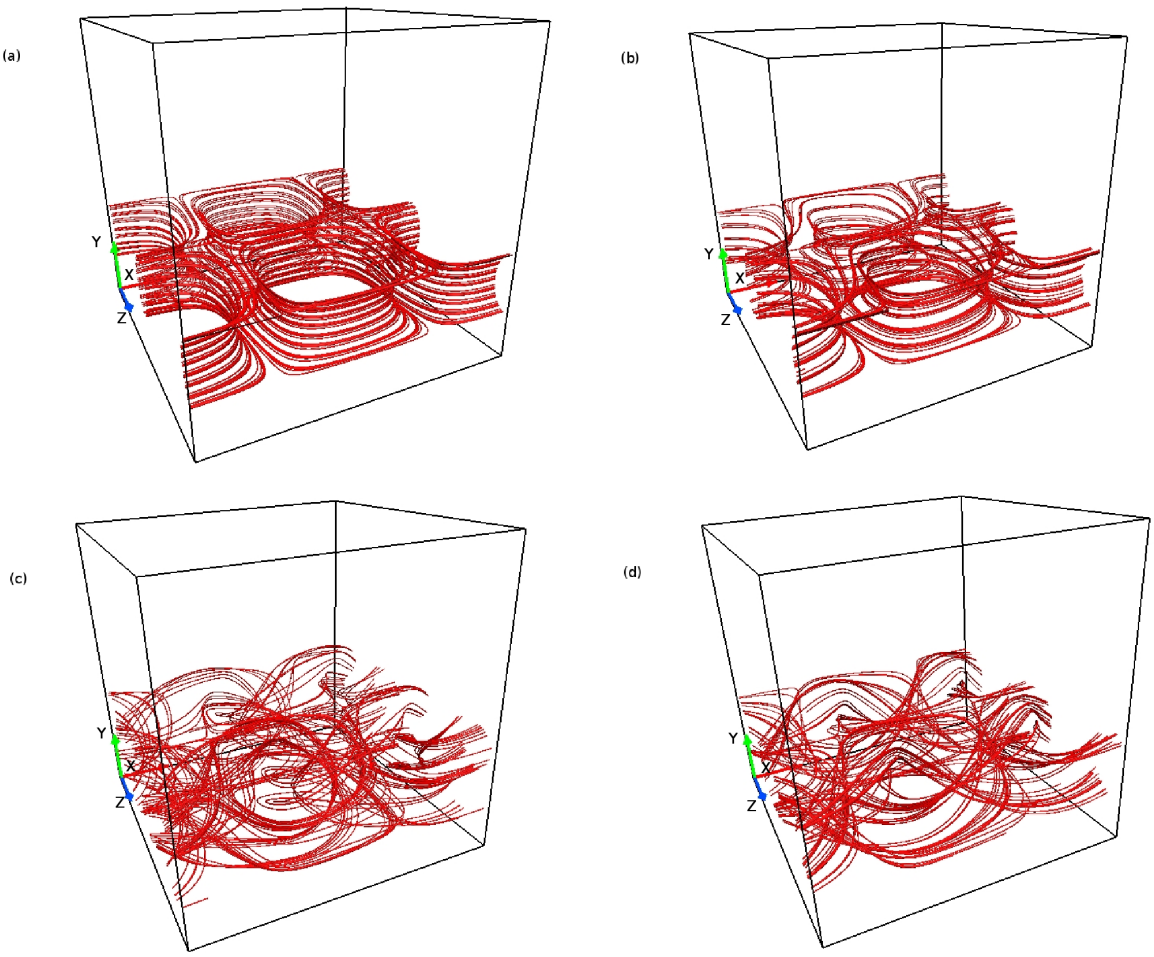

FIG. 2: The panels a, b, c and d illustrate magnetic field lines of the initial field $\mathbf{H}$ for $\epsilon_0 = 0.1, 0.3, 0.5$ and 0.7 respectively. Notably, the field lines are becoming more interlaced as ϵ_0 increases.

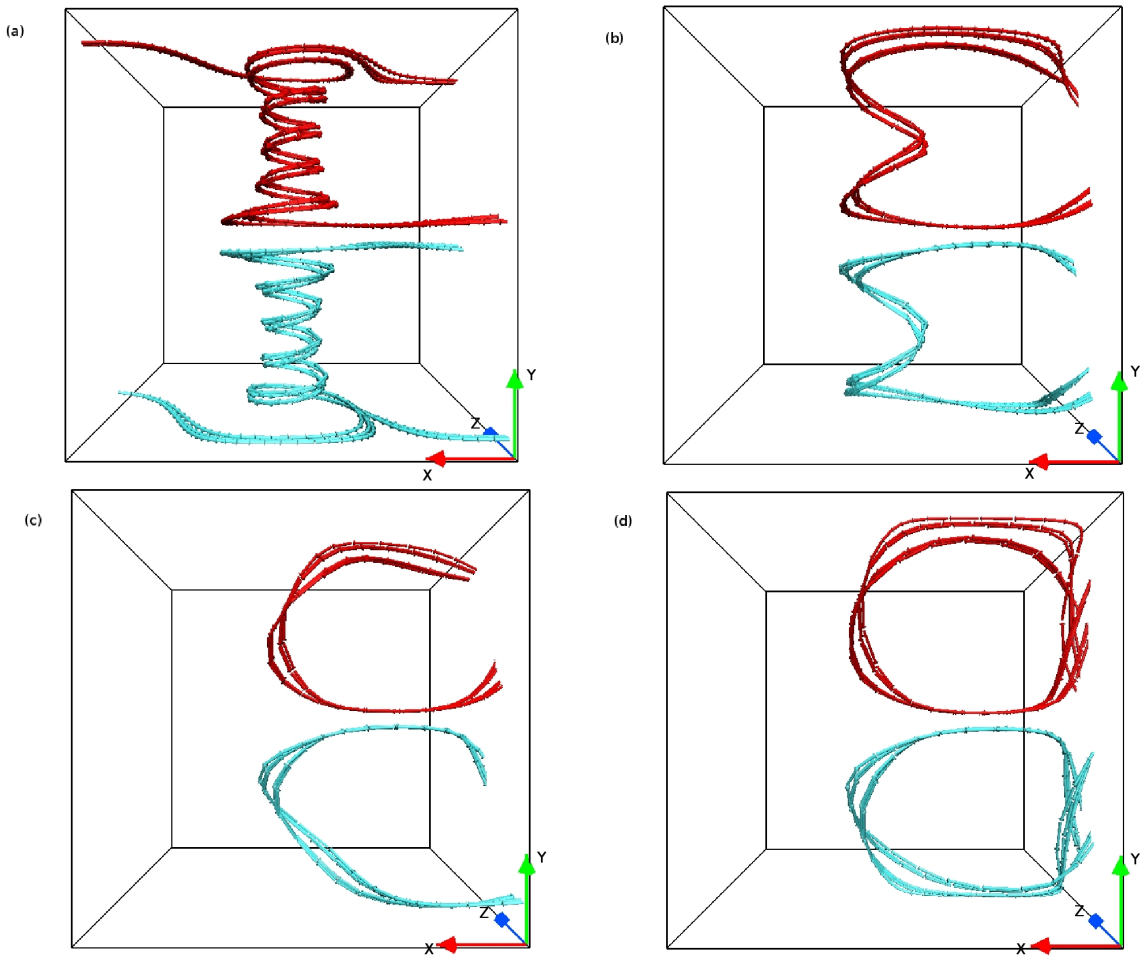

FIG. 3: Panels (a), (b), (c) and (d) show field lines of $\mathbf{H}$ for $\epsilon_0 = 0.1, 0.3, 0.5$ and 0.7 respectively. These field lines are plotted in close proximity of the $y = \pi$ plane and with $z \in \{0, \pi\}$. The figure indicates the field lines to be helical for $\epsilon_0 = 0.1$, while for larger ϵ_0, the field lines deviate from this helical structure. Importantly, the distance between two anti-parallel field lines located across the $y = \pi$ plane increases with ϵ_0.

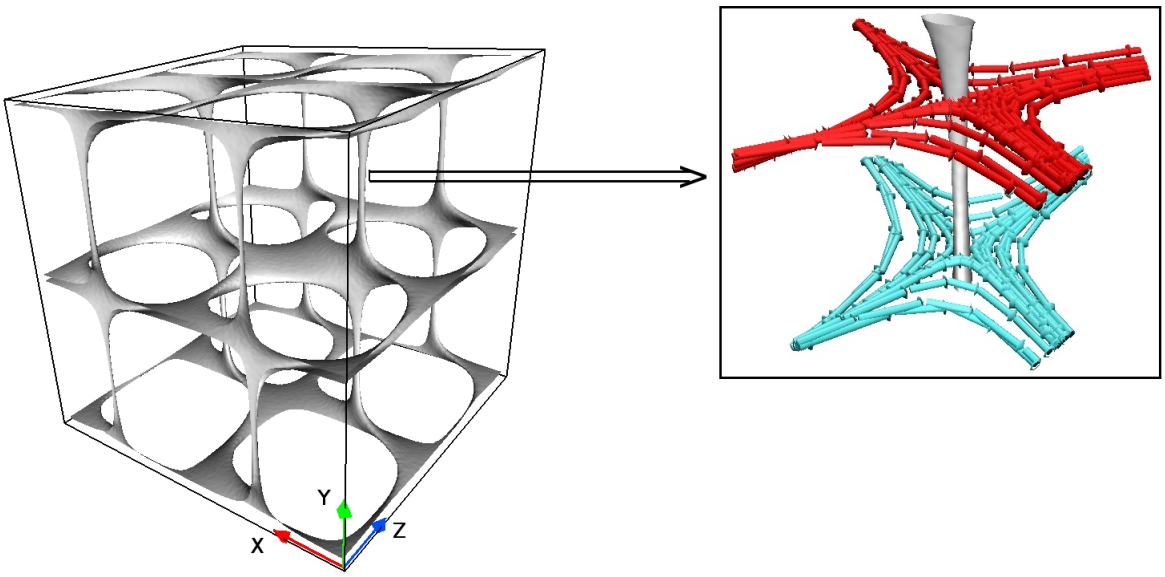

FIG. 4: The figure demonstrates the magnetic nulls by isosurfaces of $\chi(x, y, z)$, defined in (36), with parameter $H_0 = 0.01$ and $d_0 = 0.05$, for $\epsilon_0 = 0.5$. The presence of 2D nulls and complete absence of 3D nulls is evident from the figure. The field topologies near the neutral line located at $x = \pi/2$, $z = \pi$ is depicted in inset; which correspond to X-type nulls.

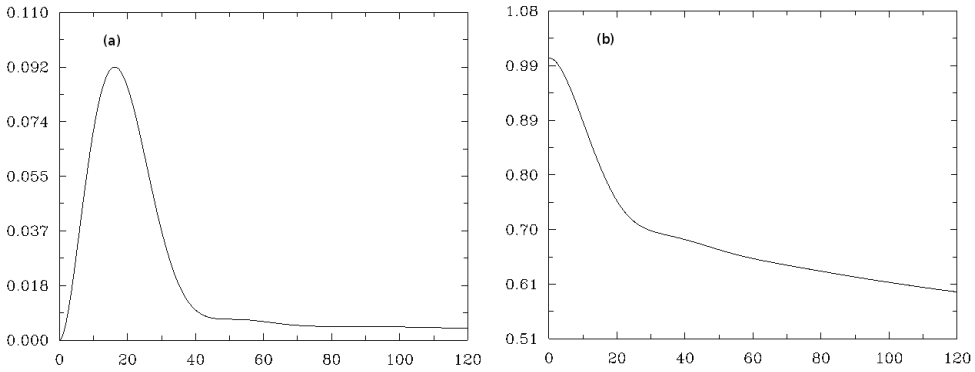

FIG. 5: Time evolution of normalized kinetic and magnetic energies for $\epsilon_0 = 0.1$ (panels *a* and *b*). The normalization is done with the initial total energy. The plots highlight the initial peak in kinetic energy and the quasi-steady phase of the evolution.

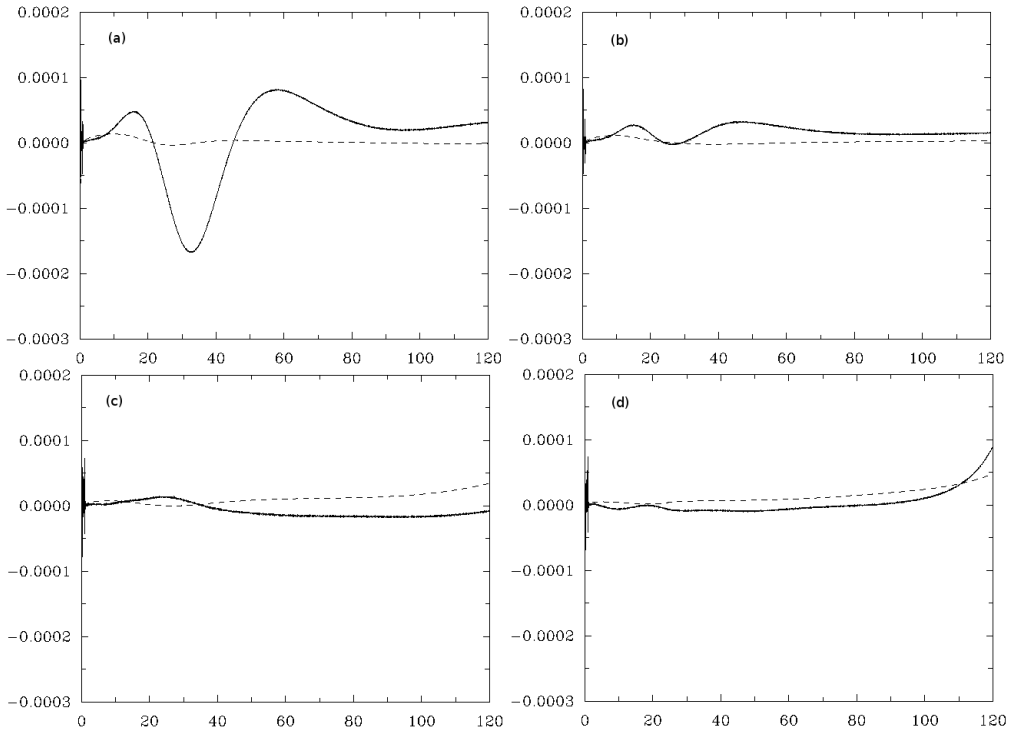

FIG. 6: Panels a, b, c, and d illustrate deviations of normalized kinetic (dashed) and magnetic (solid) energy rates from their analytical values during computations with $\epsilon_0 = 0.1, 0.3, 0.5$, and 0.7 respectively. The normalization is with respect to the initial total energy. The plots document an almost accurate maintenance of the energy rates.

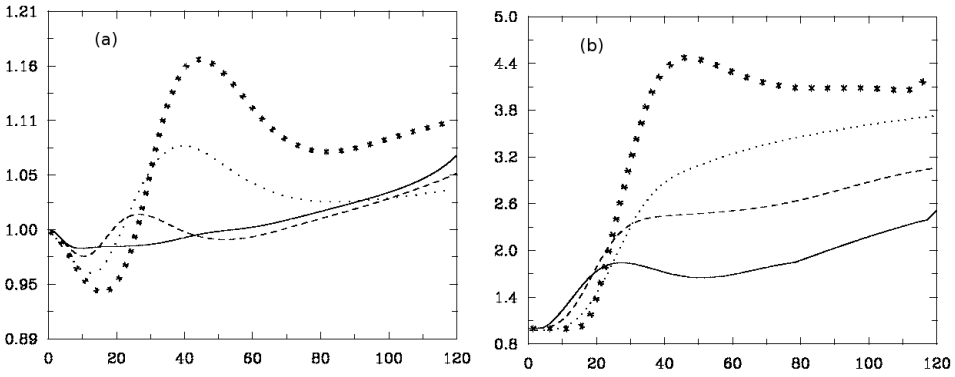

FIG. 7: Panels a and b show time evolution of normalized $<|\ \mathbf{J}\ |>$ and $J_{\max}$ respectively for $\epsilon_0 = 0.1$ (starred line), 0.3 (dotted line), 0.5 (dashed line), and 0.7 (solid line). The overall increase in current densities with time suggests development of CSs.

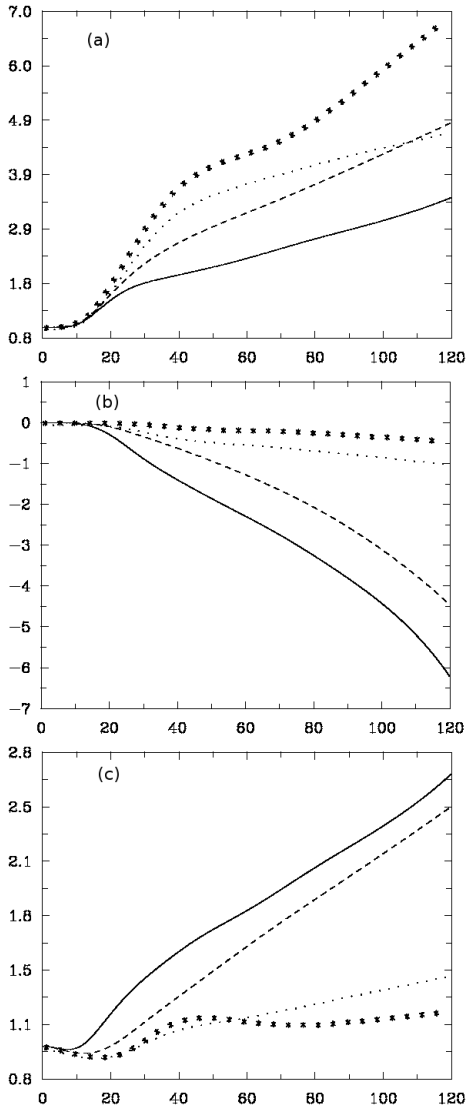

FIG. 8: Panels a, b, and c illustrate time evolution of $<|\ \mathbf{J}_2\ |>$, $<\ \mathbf{J}_1 \cdot \mathbf{J}_2\ >$, and $<|\ \mathbf{J}_1\ |>$ respectively for $\epsilon_0 = 0.1$ (starred line), 0.3 (dotted line), 0.5 (dashed line), and 0.7 (solid line). The current densities are normalized to their initial values.

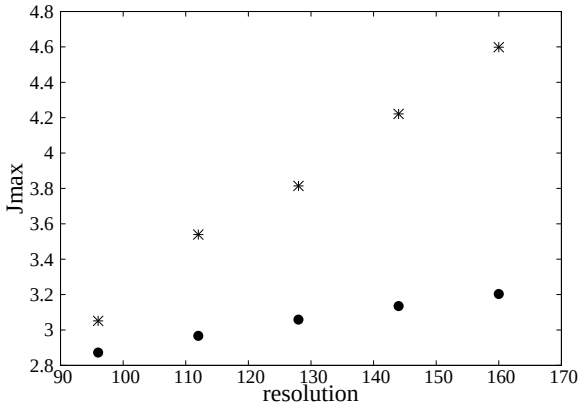

FIG. 9: The plot of $J_{\max}$ against grid resolution for $\epsilon_0 = 0.1$ (stars) and $\epsilon_0 = 0.5$ (dots). The monotonous increase of $J_{\max}$ with resolution confirms the development of CSs for both the ϵ_0 values. Also, the plot documents a stronger scaling with resolution for the case $\epsilon_0 = 0.1$.

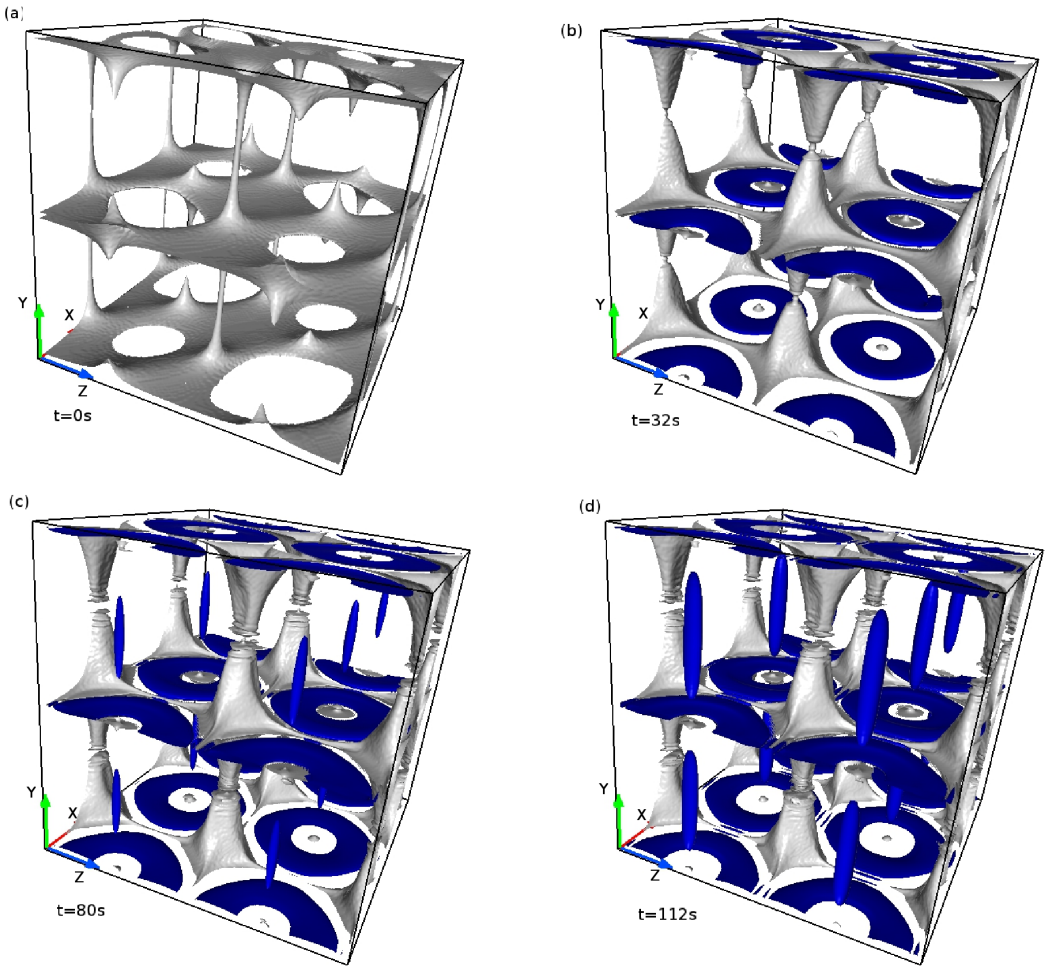

FIG. 10: Evolution of the isosurface $J - 50$ (in blue), having an isovalue which is 50% of the maximum $\mid \mathbf{J} \mid$ for $\epsilon_0 = 0.1$. The figure is further overlaid with magnetic nulls (in grey). Noteworthy is the development of CSs at $y = \pi$ plane where they are generally expected because of the presence of favorable field line topology. The figure also shows the generation of closed elongated $J - 50$ surfaces.

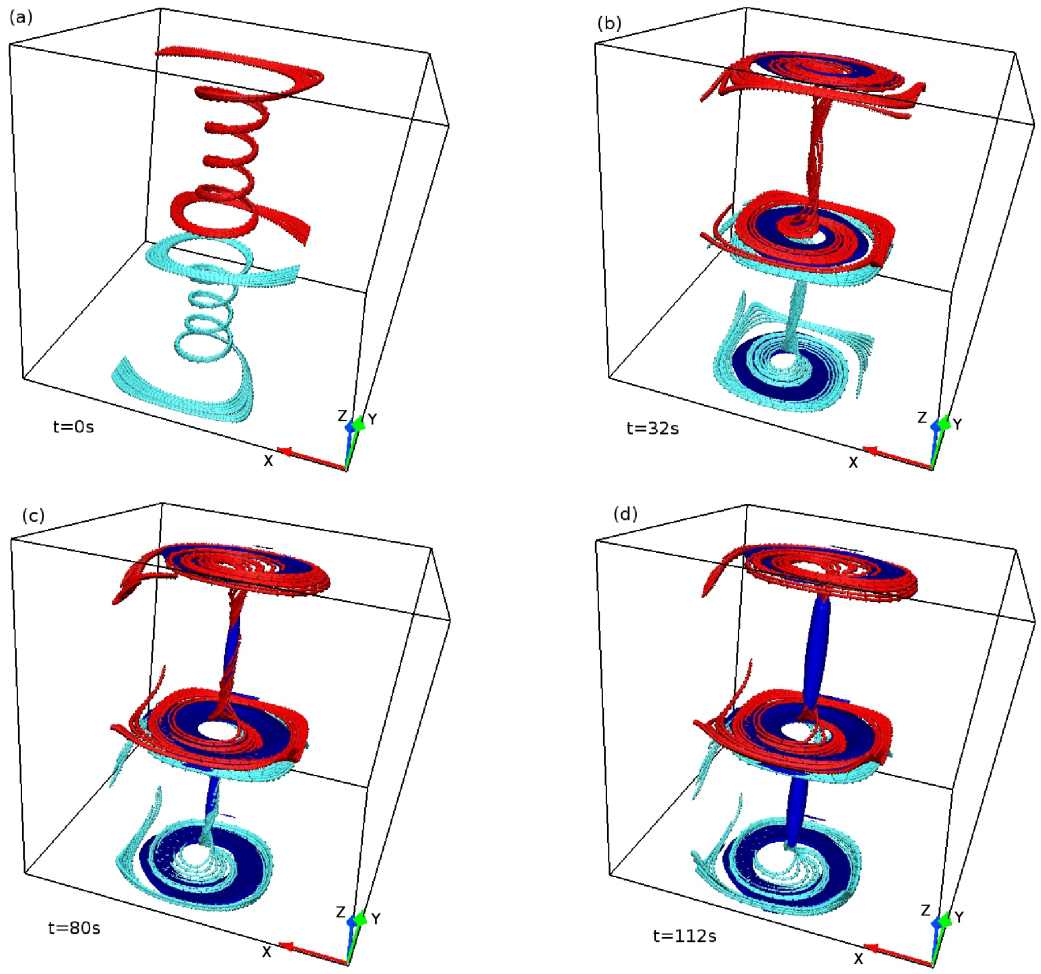

FIG. 11: History of two complementary sets of oppositely directed MFLs of the **H** along with $J-50$ surfaces (in blue) for $\epsilon_0 = 0.1$. The plots confirm development of CSs at the $y = \pi$ plane as two oppositely directed field lines approach each other. The figure also relates the closed $J-50$ surfaces to an increase in parallel field lines density, implying their onset does not indicate CS formation.

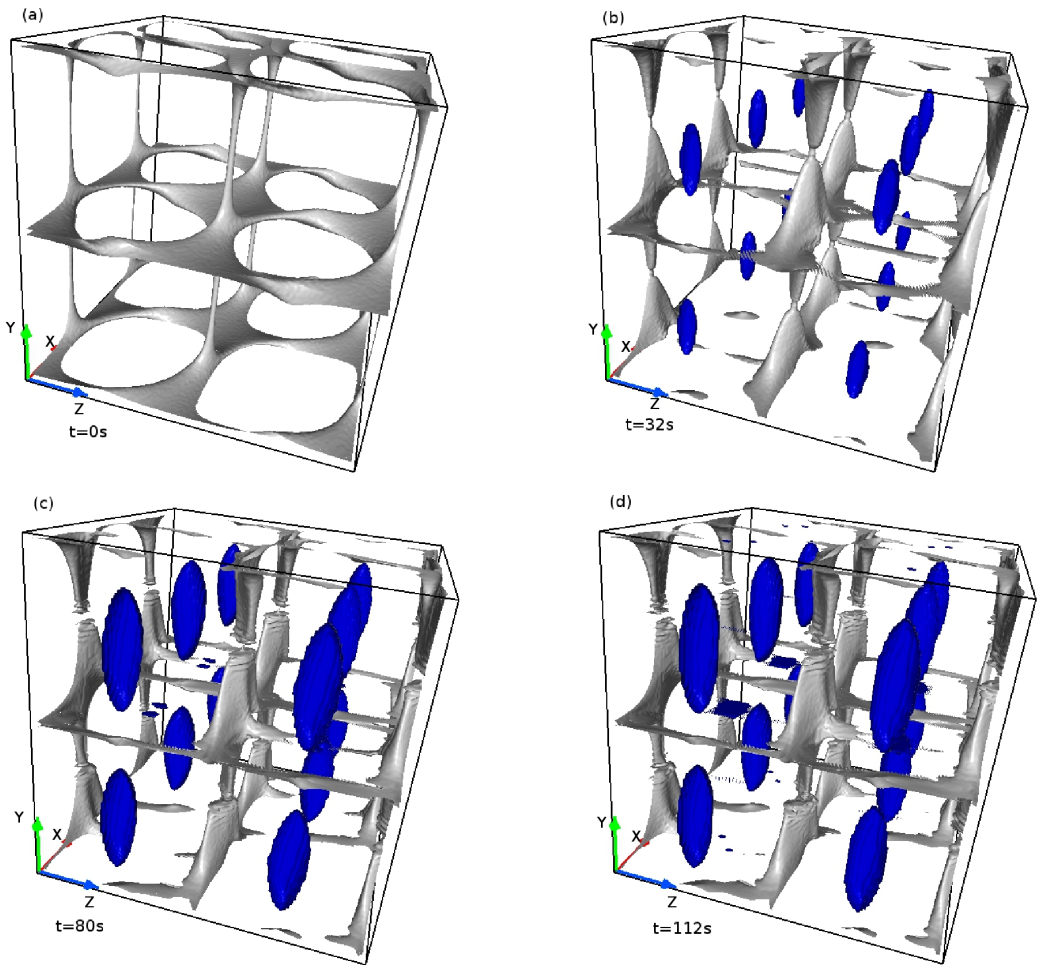

FIG. 12: Time sequence of the isosurface $J - 50$ (in blue) overlaid with magnetic nulls (in grey), for $\epsilon_0 = 0.3$. The plots illustrate the appearances of closed elongated current structures along with CSs located at the $y = \pi$ plane.

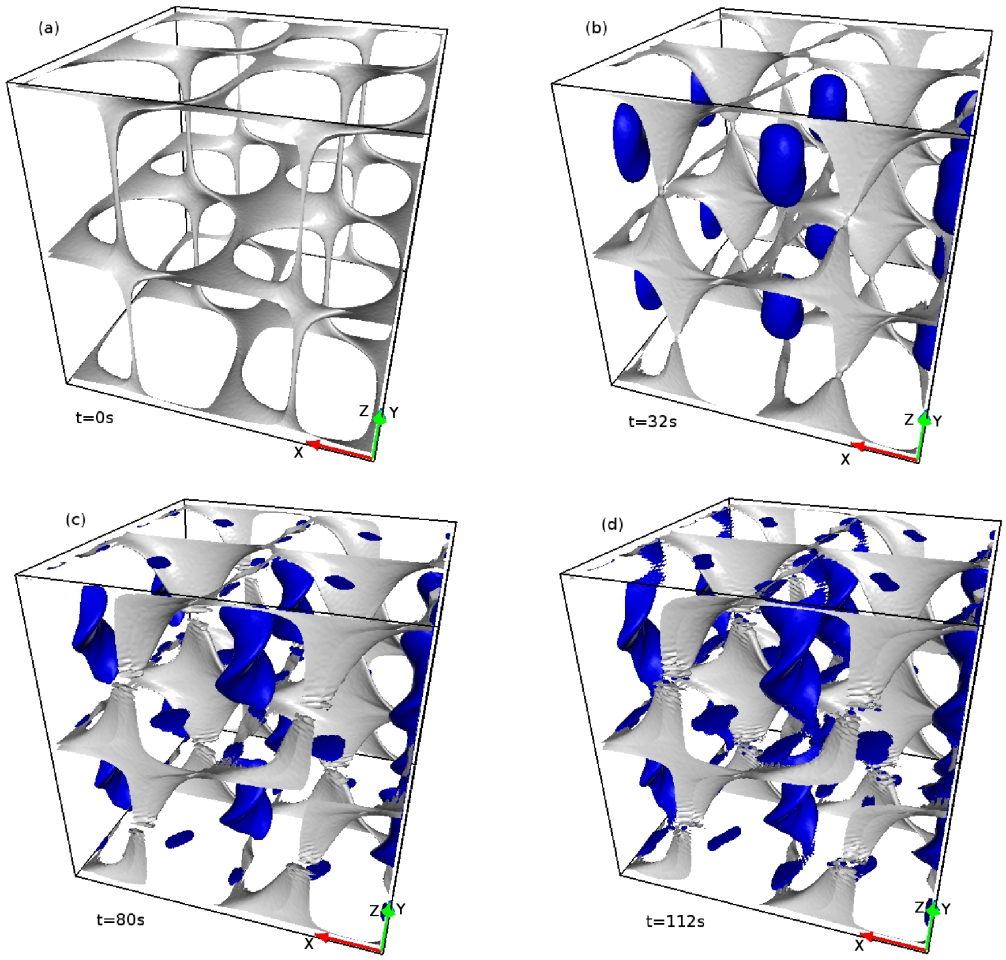

FIG. 13: Evolution of the surface $J - 50$ (in blue) overlaid with magnetic nulls (in grey), for $\epsilon_0 = 0.5$. Noteworthy is the development of CSs away from the nulls.

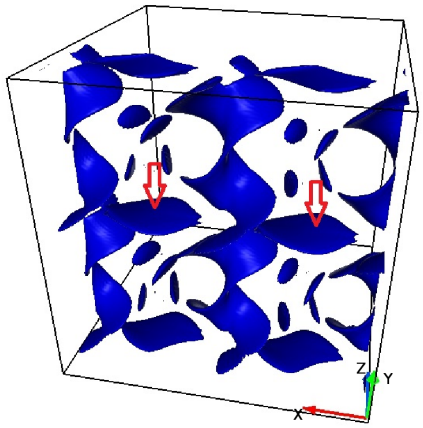

FIG. 14: Appearance of $J_1 - 40$ surfaces at $t = 112s$ for $\epsilon_0 = 0.5$, plotted in the half computational domain with $z \in \{0, \pi\}$. The $J_1 - 40$ surfaces are comprised of helices extended along the y axis and patches (marked by downward arrows) located at the $y = \pi$ plane.

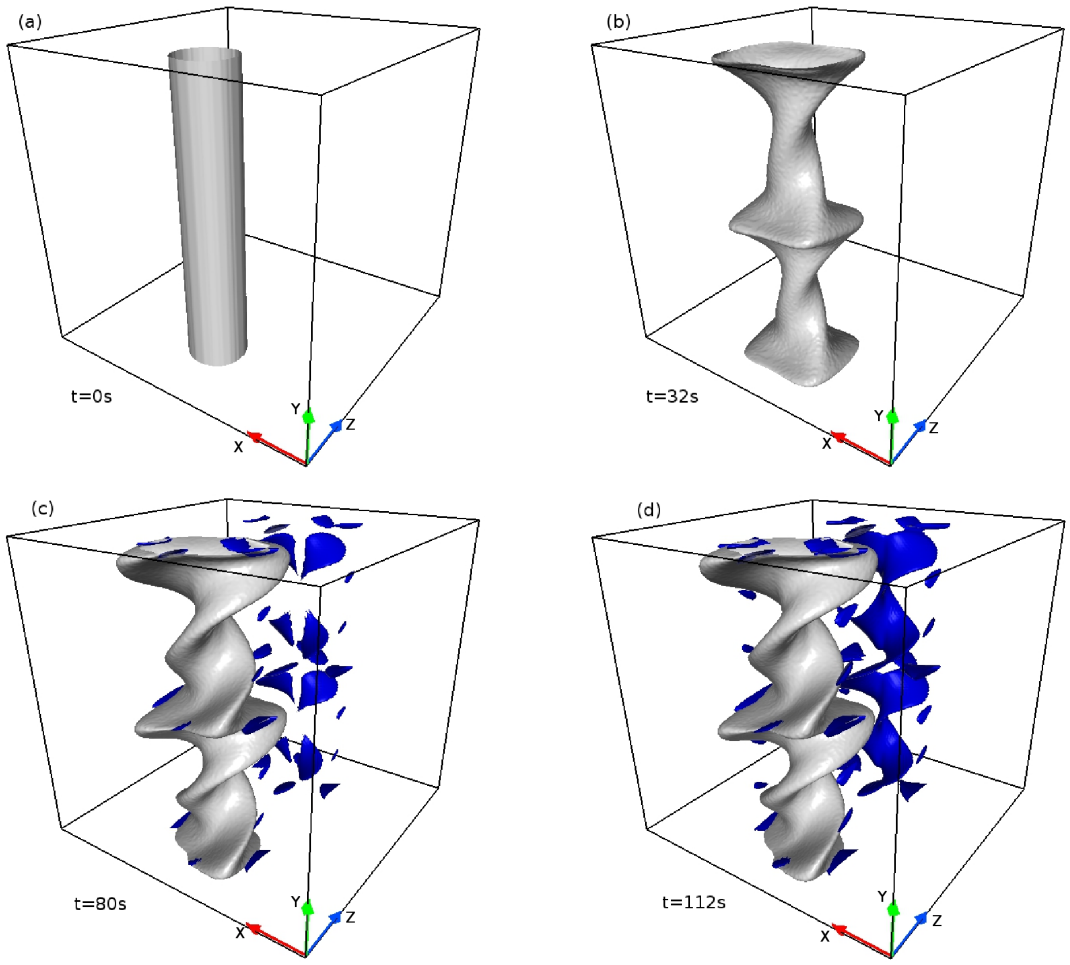

FIG. 15: Evolution of Euler surface $\psi_1 = -0.65$ (in grey) overlaid with the $J_1 - 40$ surface (in blue), for $\epsilon_0 = 0.5$. For better visualization, the evolution is shown in the subdomain $x \in \{\frac{2\pi}{3}, \frac{4\pi}{3}\}$. Noteworthy, the $J_1 - 40$ surface is co-located with the contortion of $\psi_1 = -0.65$ surface, inferring the causality between them.

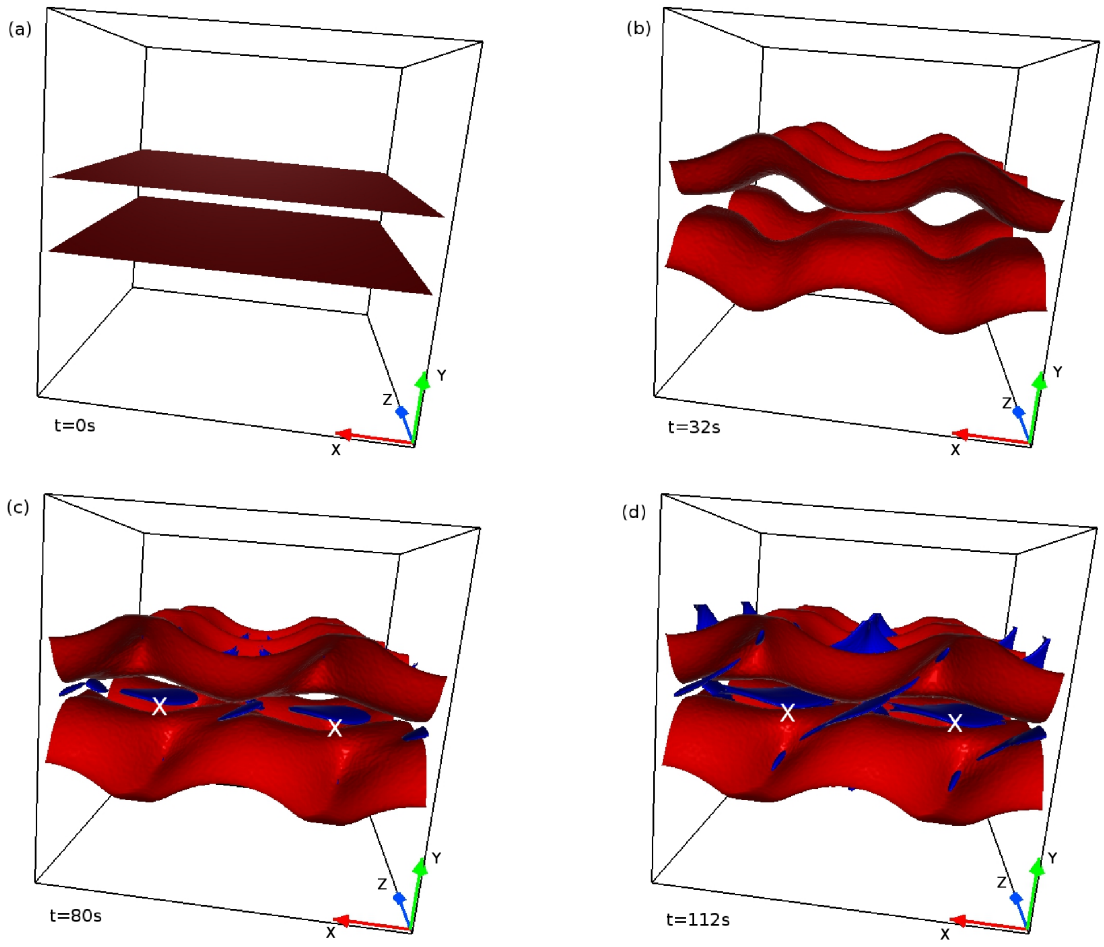

FIG. 16: Time profile of Euler surfaces $\phi_1 = -0.60$ (in red) overlaid with the surface $J_1 - 40$ (in blue) for $\epsilon_0 = 0.5$, plotted in a selected portion of the computational domain. The two Euler surfaces depicted in the figure reside on two opposite sides of the $y = \pi$ plane. The figure identifies the development of current patches (marked by X) to favorable contortions of ϕ_1.

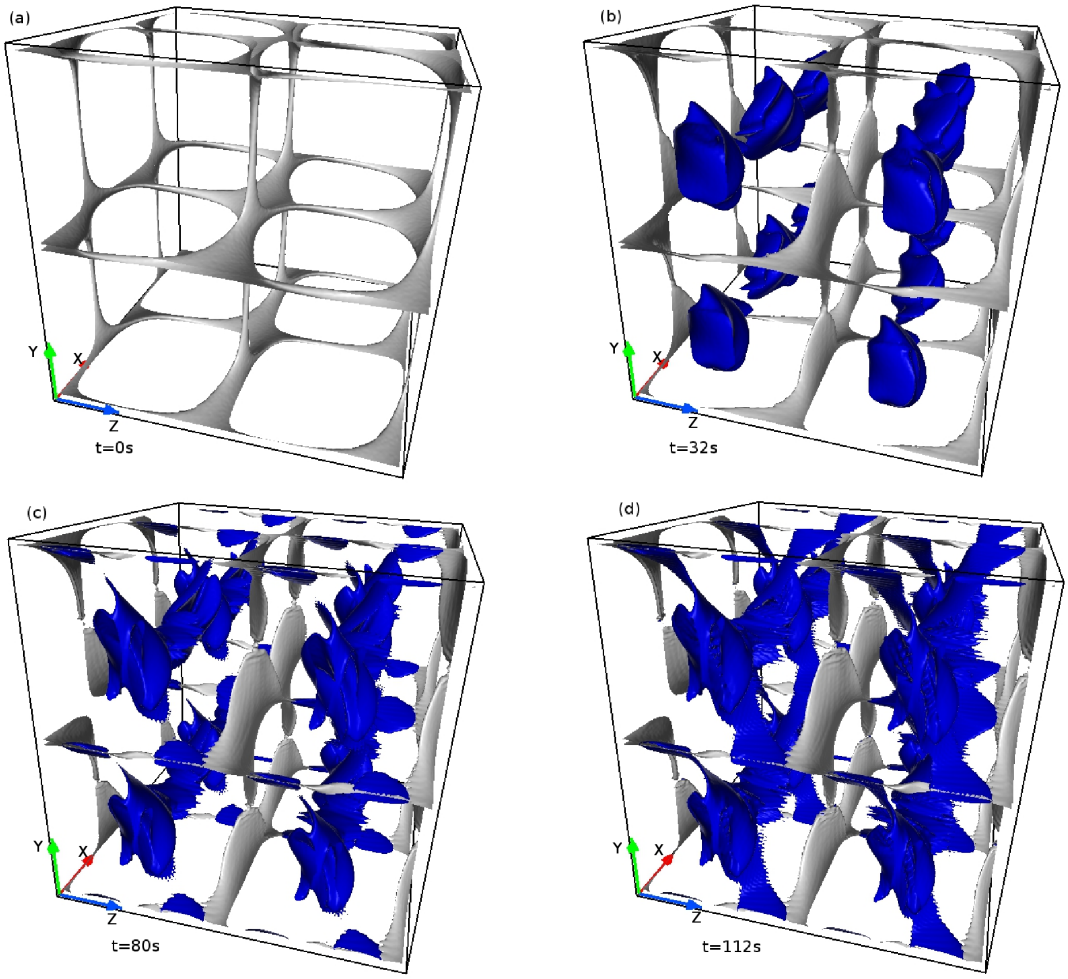

FIG. 17: Development of the surface $J - 50$ (in blue) overlaid with magnetic nulls (in grey), for $\epsilon_0 = 0.7$. The figure substantiates onset of CSs which are away from magnetic nulls and the $y = \pi$ plane. Furthermore, these CSs are distributed through out the computation volume.

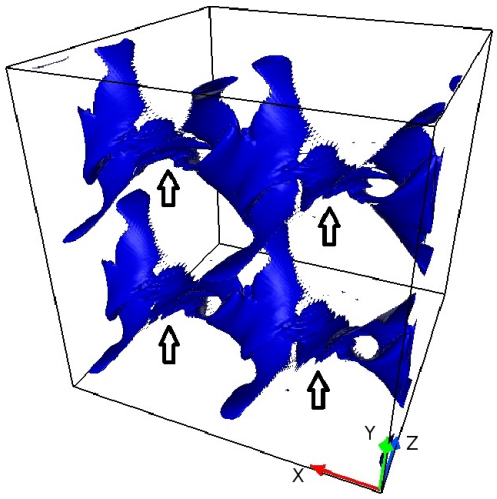

FIG. 18: A snapshot of the $J-50$ surfaces at $t = 112s$, for $\epsilon_0 = 0.7$. The surfaces are plotted in the half computational domain with $z \in \{0, \pi\}$. From the figure, evident are the helical CSs extending along the y axis and the current patches (marked by upward arrows) tangential to y-constant planes.

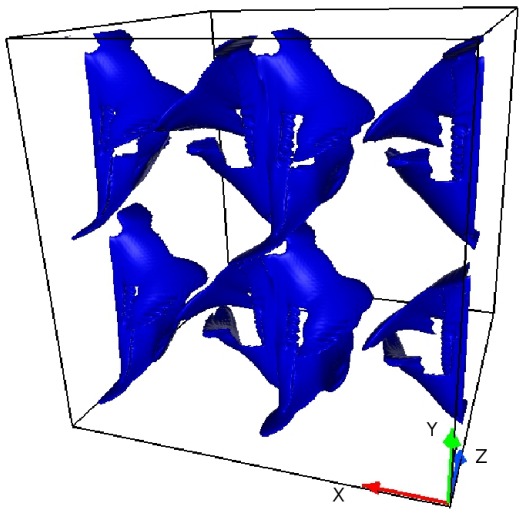

FIG. 19: Appearances of $J_1 - 40$ surface at $t = 112s$ for $\epsilon_0 = 0.7$, depicted in the half computational domain with $z \in \{0, \pi\}$. The $J_1 - 40$ surfaces are elongated along the y axis.

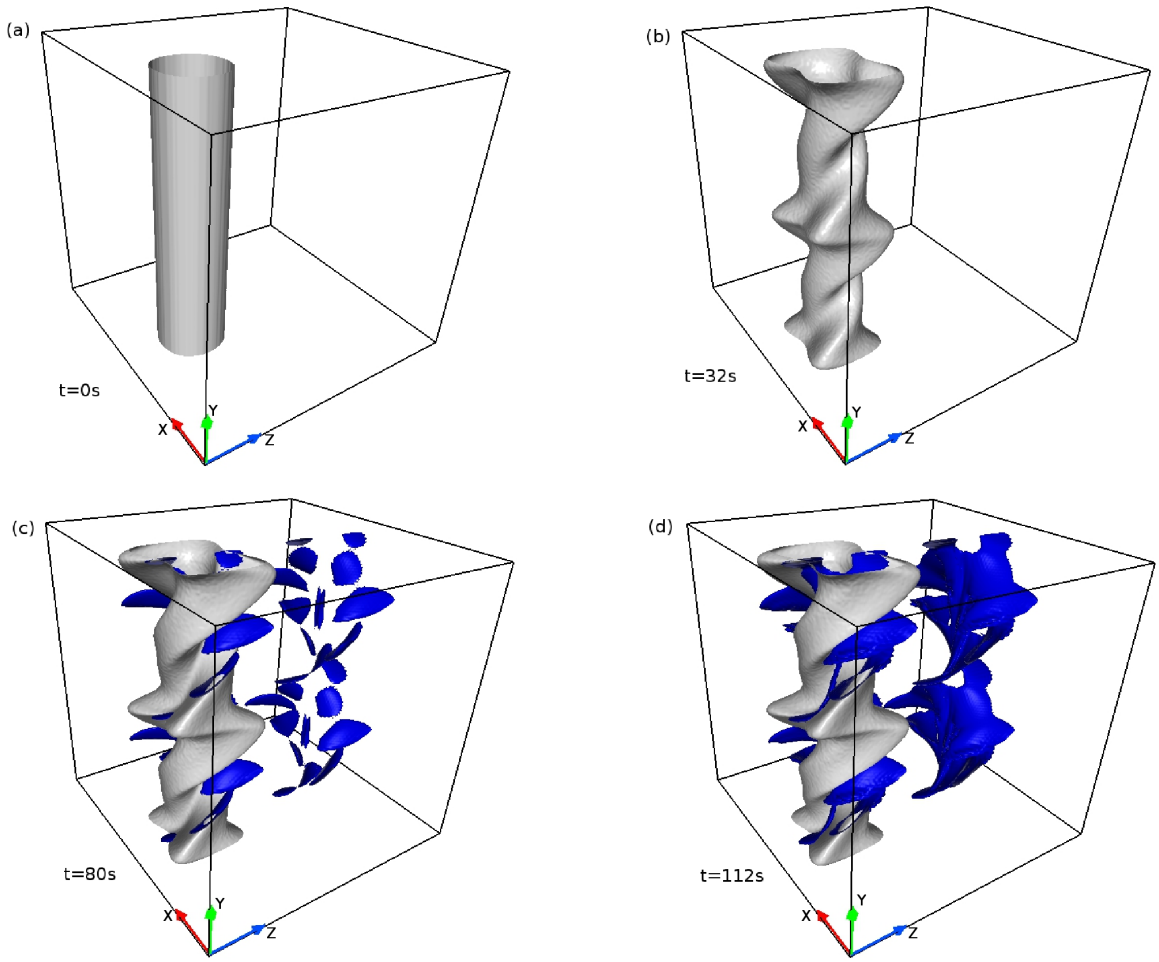

FIG. 20: Evolution of Euler surfaces $\psi_1 = -0.60$ (in grey) overplotted with the surface $J_1 - 40$ (in blue) for $\epsilon_0 = 0.7$, shown in the computational domain with $x \in \{\frac{2\pi}{3}, \frac{4\pi}{3}\}$. The figure indicates contortions of ψ_1-constant Euler surfaces to be responsible for onset of the helical $J_1 - 40$ surfaces.

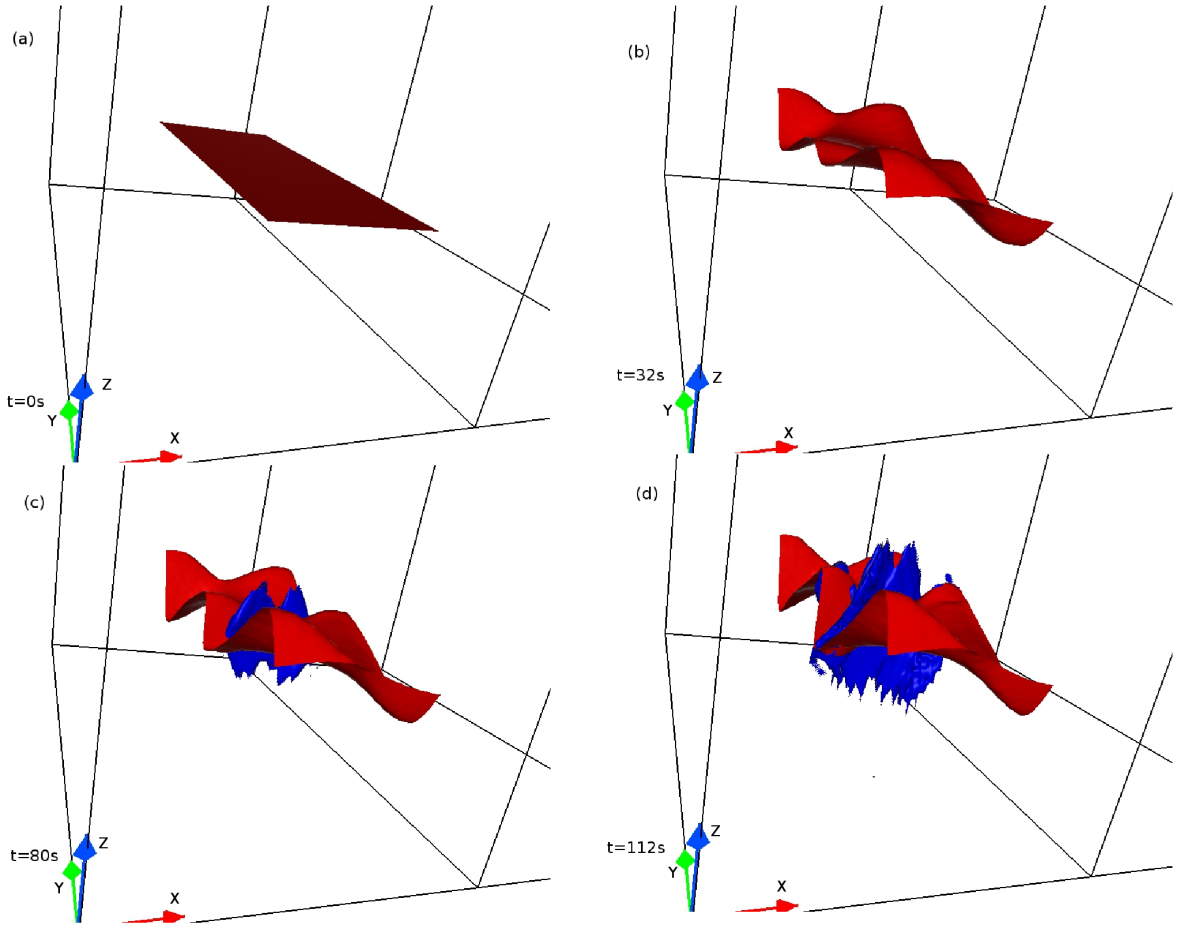

FIG. 21: Evolution of Euler surfaces $\phi_2 = 0.05$ (in red) overlaid with the surface $J_2 - 40$ (in blue) for $\epsilon_0 = 0.7$. The figure indicates, contortions of the ϕ_2-constant surfaces are responsible for developing the patches of $J_2 - 40$ tangential to y-constant planes.

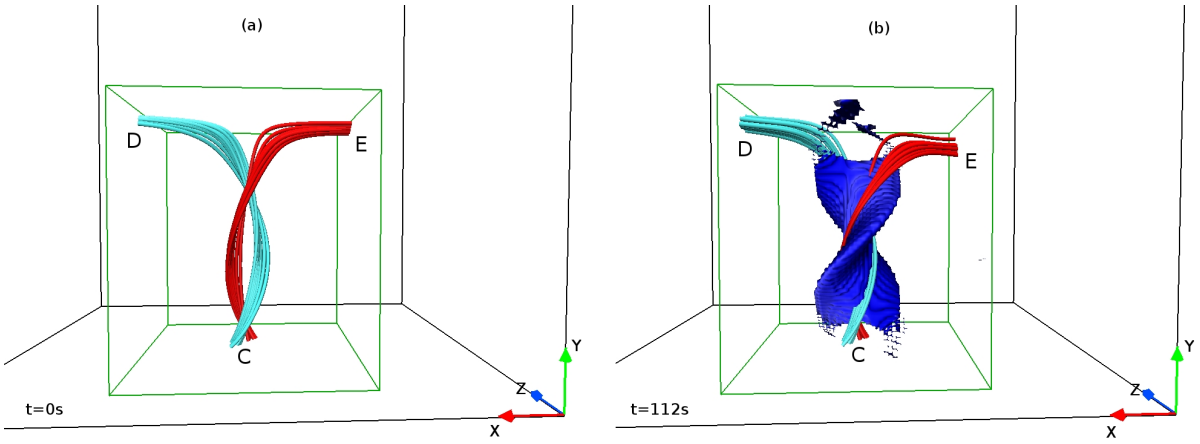

FIG. 22: Two sets of MFLs (colored red and cyan) **H** overlaid with the $J - 50$ surfaces (in blue) at $t = 0s$ and $t = 112s$, for $\epsilon_0 = 0.5$. The bifurcation of the MFLs, with the red set connecting the planes C and E and the cyan set connecting the planes C and D, documents a change in field line connectivity. The appearances of CS (in blue) co-located to the layers across which the MFLs bifurcate, suggest the presence of QSL structures in **H**. Additionally, the MFLs at $t = 112s$ (with the CS fully develop) are more helical compared to the MFLs at $t = 0s$ (in absence of CS); indicating a causal connection between the favorable contortions and the dynamics of QSLs.